



## Network connectivity modulates power spectrum scale invariance



Anca Rădulescu<sup>a</sup>, Lilianne R. Mujica-Parodi<sup>b,c,\*</sup>

<sup>a</sup> Department of Mathematics, University of Colorado, 395 UCB, Boulder, CO 80309-0395, USA

<sup>b</sup> Department of Biomedical Engineering, Stony Brook University, Stony Brook, NY 11794-5281, USA

<sup>c</sup> Department of Radiology, A. A. Martinos Center for Biomedical Imaging, Massachusetts General Hospital, Charlestown, MA 02129, USA

### ARTICLE INFO

#### Article history:

Accepted 3 December 2013

Available online 13 December 2013

### ABSTRACT

Measures of complexity are sensitive in detecting disease, which has made them attractive candidates for diagnostic biomarkers; one complexity measure that has shown promise in fMRI is power spectrum scale invariance (PSSI). Even if scale-free features of neuroimaging turn out to be diagnostically useful, however, their underlying neurobiological basis is poorly understood. Using modeling and simulations of a schematic prefrontal-limbic meso-circuit, with excitatory and inhibitory networks of nodes, we present here a framework for how network density within a control system can affect the complexity of signal outputs. Our model demonstrates that scale-free behavior, similar to that observed in fMRI PSSI data, can be obtained for sufficiently large networks in a context as simple as a linear stochastic system of differential equations, although the scale-free range improves when introducing more realistic, nonlinear behavior in the system. PSSI values (reflective of complexity) vary as a function of both input type (excitatory, inhibitory) and input density (mean number of long-range connections, or strength), independent of their node-specific geometric distribution. Signals show pink noise ( $1/f$ ) behavior when excitatory and inhibitory influences are balanced. As excitatory inputs are increased and decreased, signals shift towards white and brown noise, respectively. As inhibitory inputs are increased and decreased, signals shift towards brown and white noise, respectively. The results hold qualitatively at the hemodynamic scale, which we modeled by introducing a neurovascular component. Comparing hemodynamic simulation results to fMRI PSSI results from 96 individuals across a wide spectrum of anxiety-levels, we show how our model can generate concrete and testable hypotheses for understanding how connectivity affects regulation of meso-circuits in the brain.

© 2013 Elsevier Inc. All rights reserved.

### Introduction

Measures of complexity are sensitive in detecting disease, which has made them attractive candidates for diagnostic biomarkers. One straightforward way of characterizing complexity is the use of power spectrum scale invariance (PSSI), which measures the relative frequency content of signals whose spectra show power law behavior:  $S(f) \propto f^\beta$ . In this context, the scaling exponent  $\beta$  is 0 (white-noise) at maximum entropy, with  $\beta = -1, -2$  representing the increasing regularity of pink and brown noise respectively. To date, several studies have applied complexity analyses to fMRI, and have shown that for healthy neurobiological states, the entropy of neural time-series is characterized by roughly  $\beta = -1$  ( $S(f) \propto 1/f$ ), while neural time series in schizophrenia (Rădulescu et al., 2012), anxiety (Tolkunov et al., 2010), and autism (Lai et al., 2010), show a significant shift towards  $\beta = 0$ . In contrast, EEG signals from patients with epilepsy also deviate from the pink noise range, but in this case towards greater regularity (Bhattacharya et al., 2000; Bruzzo et al., 2008; Molteni et al., 2008; Protzner et al., 2010). The fact

that complexity should be able to identify disease states is not unique to the brain: the diagnostic use of fractals and complexity as applied to ECG has a long-standing history in physiology, most particularly in its application of heart-rate variability (HRV) to detect risk for myocardial infarction and heart disease (Cerutti et al., 2009; Ho et al., 1997; Kaplan et al., 1991; Li et al., 2007; Mäkilallio et al., 1998; Mujica-Parodi et al., 2005; Peng et al., 1994; Pincus and Goldberger, 1994; Stanley et al., 1992; Valencia et al., 2009; Voss et al., 1995).

Even if spectral power law features of neuroimaging turn out to be diagnostically useful, however, their underlying neurobiological basis is poorly understood. In the case of HRV, complexity in the healthy heart-rate is assumed to be a consequence of autonomic control. A healthy autonomic nervous system has excitatory (primarily sympathetic) and inhibitory (primarily parasympathetic) components that work in tandem, ensuring a system that is supple enough to easily respond to even small stimuli, yet constrained enough to efficiently return to baseline. Thus, the fact that healthy heart rates fall in the pink noise range (Peng et al., 1993, 1995), balanced between chaos and order, seems intuitive not only from a physical and dynamical systems perspective, in which pink noise is associated with the metastable point at which phase transitions occur (Gisiger, 2001), but also as a physiologically-plausible consequence of negative feedback.

\* Corresponding author at: Program in Neuroscience, Stony Brook University, Stony Brook, NY 11794-5230, USA. Tel.: +1 631 632 1008.

E-mail address: [lilianne.strey@stonybrook.edu](mailto:lilianne.strey@stonybrook.edu) (L.R. Mujica-Parodi).

Unlike the autonomic nervous system, however, the brain's networks (at multiple scales) are still very much in the early stages of being defined, and thus present a much greater challenge in terms of identifying their relationship to the complexity of measured electrophysiological or hemodynamic signals. Nevertheless, and in spite of numerous parallel pathways within the system, there do appear to be meso-circuits that have predominant excitatory and inhibitory components, and that function at scales measurable in the awake animal and human. One such meso-circuit is the prefrontal-limbic system, for which the amygdala and prefrontal (orbitofrontal, ventromedial, dorso-lateral) regions provide up and down-regulation of the emotional arousal response, respectively (Baxter et al., 2000; Davis et al., 2001; Izquierdo and Murray, 2005; LeDoux, 2000; Mujica-Parodi et al., 2009; Phelps et al., 2004; Rosenkranz et al., 2003; Sotres-Bayon et al., 2006).

Recent studies have used random network approaches to investigate the organizational principles of brain networks (Bullmore and Sporns, 2009), with nodes and edges defined according to modality appropriate scales (Sporns, 2010). Since the temporal evolution of a network is expected to depend on a combination of its hardwired circuitry and its dynamic coupling, much work has been directed towards understanding the effect of the neural architecture on neural function (Boccaletti et al., 2006). The stability and synchronization patterns of brain networks with coupled randomly distributed excitatory and inhibitory neural populations have been investigated, both analytically and numerically, in a variety of contexts: from biophysical models (Gray and Robinson, 2008), to simplified systems (Siri et al., 2007). These analyses reveal a rich range of potential dynamic regimes and transitions (Brunel, 2000), shown to depend as much on the coupling parameters of the network as on the arrangement of the excitatory and inhibitory connections (Gray and Robinson, 2009). In fact, from a graph theoretical perspective, studies support certain generic topological properties of the human brain architecture, such as modularity, small-worldness, the existence of hubs and other connectivity density patterns (He and Evans, 2010).

Here, we take a similar random network based approach to investigate general constraints on how dynamic activity can emerge and be modulated by connectivity between excitatory and inhibitory nodes in a meso-circuit with feedback (e.g., the prefrontal-limbic system), viewed as a network of hemodynamic nodes relevant to fMRI studies. Using modeling and simulations, we present a framework for how network density within our control system can affect the complexity of signal outputs. We build upon our previous black-box models (Rădulescu, 2008, 2009), to include two interconnected brain networks, one excitatory and the other inhibitory. The model was designed within the constraints of three broad parameters. First, it needed to be simple enough to analyze mathematically as well as to simulate using reasonably-sized (~10<sup>2</sup>-node) networks. Second, it needed to be multi-layered, such that, at the hemodynamic scale, networks of nodes could be nested within the interaction of the two primary brain regions. Third, the model should schematically represent the prefrontal-limbic system in order to inform our neuroimaging results of that same system, but constraints should be sufficiently general to maintain relevance for other neural control circuits. With this last goal in mind, we chose to incorporate a neurovascular component and to characterize complexity using PSSI, to permit comparison with prior fMRI results (Lai et al., 2010; Rădulescu et al., 2012; Tolkunov et al., 2010).

The general aim was to provide a theoretical bridge between deviations in signal complexity measured at the hemodynamic scale, and the connectivity that might underlie it. Because many different models can produce the same behavior, it is not possible to use behavior to “test” whether a model is correct. Nevertheless, models can provide a way to determine whether certain types of parameters and their interactions are capable of leading to certain kinds of outcomes, generating well-defined hypotheses that can then be tested empirically. In this case, we wanted to identify a (neurobiologically-plausible, testable) mechanism that might explain how network properties in a control system

affect the distribution of frequencies (complexity) of signal outputs. While the control structure is not unique to the prefrontal-limbic system, our reference to that meso-circuit was motivated by two considerations. First, animal and human experiments had already identified excitatory and inhibitory components, making it a reasonable candidate for control systems modeling. Second, we hoped that it might be able to inform our results from two fMRI studies of healthy individuals, one on stress vulnerability and the other on stress resilience, which together showed a consistent pattern between PSSI of the prefrontal-limbic system and susceptibility to anxiety.

## Methods

### Modeling methods

In our model, we construct two interacting networks of nodes, such that each node is self-damping, interacts locally with all others within its module (thus obtaining some degree of modular internal synchronization) and also has long-range connections with a variable fraction of the nodes in the opposite module (Fig. 1).

We represent these two interacting networks, module X and module Y, by two sets of variables:  $x_k, k = 1, \dots, N$  and  $y_k, k = 1, \dots, N$  respectively, obeying the constraints described by the following system of 2  $N$  first order linear differential equations:

$$\begin{aligned} \frac{dx_k}{dt} &= -\gamma_x x_k + \sum_{p=1}^N g_{yx} A_{kp} (y_p - x_k) + \sum_{p=1}^N g_{xx} (x_p - x_k) + I_k(t) \\ \frac{dy_k}{dt} &= -\gamma_y y_k + \sum_{p=1}^N g_{xy} B_{kp} (x_p - y_k) + \sum_{p=1}^N g_{yy} (y_p - y_k), \end{aligned} \tag{1}$$

where the parameters represent the following:  $\gamma_x$  and  $\gamma_y$  are damping coefficients,  $g_{xx}$  and  $g_{yy}$  are local connection strengths, assumed to be the same within each module;  $g_{xy}$  and  $g_{yx}$  are long-range connection strengths (from nodes in X to nodes in Y, and conversely). The damping coefficients guarantee the decay to zero of solutions in absence of external forcing terms. These parameters can be drawn more generally from prescribed distributions of values (see the Modeling nonlinearity section); in this section, however, we use for each type of parameter a fixed (mean) value, in order to keep our formal calculation of the spectra more tractable.  $M_{xy}$  and  $M_{yx}$  represent densities of edges between X and Y. More precisely, one can define  $\alpha$  to be the number of oriented edges from nodes in X to nodes in Y, and  $\delta$  to be the number of oriented edges from nodes in Y to nodes in X, so that  $0 \leq \alpha, \delta \leq N^2$ . We consider the corresponding edge densities to be normalized as  $M_{xy} = \alpha/N^2$  and  $M_{yx} = \delta/N^2$ , so that  $0 \leq M_{xy} \leq M_{yx} \leq 1$ . Note that the densities  $M_{xy}$  and  $M_{yx}$  are fractions (or percentages) of  $N^2$ , which represent the maximum number of edges that could run from each module to the opposite one.

The equations were inspired by a system of coupled springs, in which the driving force imposed on each spring by another with

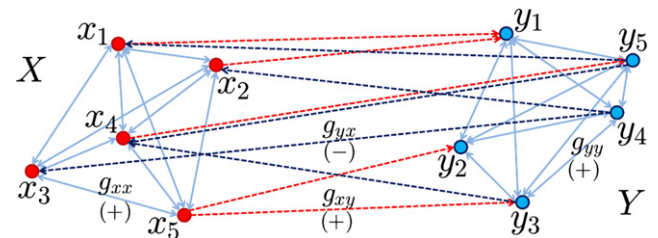


**Fig. 1.** Schematic representation of bimodular network for  $N = 5$  nodes per module. The excitatory neural population X is shown on the left; the inhibitory population Y is shown on the right. They are both fully-connected, local sub-graphs of the full network. The dotted red arrows represent the long-range X–Y connections, and the dotted blue arrows represent the Y–X connections, all generated randomly for low feed-forward and feedback connectivity densities  $M_{yx} = M_{xy} = 25\%$ , to maintain clarity of the illustration.

which it is coupled is proportional to the difference between their current amplitudes. That is, in our system the state of a given node is influenced positively or negatively by the nodes that are connected to it by edges, depending on the level of activity in each, and on the nature of the connection (excitatory or inhibitory). Notice that, formally, the subtractive terms can be easily absorbed within the damping of each equation when writing the system's Jacobian.

The matrices  $A = (A_{kp})$  and  $B = (B_{kp})$  are binary matrices representing which of the cells in  $X$  are cross-connected with cells in  $Y$  and conversely. They were generated randomly for each numerical simulation, for fixed densities  $M_{xy}$  and  $M_{yx}$ .

In addition to the neural contributions described in the system (7), the nodes in module  $X$  were each subject to external forcing terms  $I_k(t) = \hat{I}(t) + i_k(t)$ ,  $k = 1, \dots, N$ , in the form of white noise (representing exogenous inputs via sensory pathways). The inputs had two white noise components: one channel  $\hat{I}(t)$  of amplitude 0.01 common to all nodes, representing the actual signal, and a node-specific white noise jitter  $i_k(t)$  of amplitude 0.005, representing variability among the nodes' reception of a common signal.

This random input introduced a stochastic component in an otherwise simple deterministic system with trivial long-term behavior. We solved the system numerically, using the Euler–Maruyama method for integrating SDEs (Kloeden et al., 1994), with a fixed step size  $h = 2.5$  s (units are taken to be seconds, as per our experimental data). Because the system has strong self-damping, the discrete solutions (time series) obtained by numerical integration have a short transient decay, after which they settle to mainly noise-driven oscillations. We allowed the solutions to settle for  $\tau = 25$  s (i.e., 10 data-points), then “recorded” time series of length  $\tau = 750$  s (i.e., 300 data points), which we used for our further analysis. While remaining in a range of parameters that ensures convergence of the algorithm, we aimed to generate and analyze our model time series within a setup as close as possible to that used when processing the empirical time series (see below). We chose the step size in accordance with the time resolution used in our experimental recordings, and the series length to be comparable to that of our typical fMRI time series (~300 data points). Likewise, we did not artificially reduce noise by considering longer simulations or averaging multiple runs. Rather, we found that presenting the statistics (within each module and over multiple runs) was more informative, illustrating not just the mean slope values, but also the connectivity effects on their variability. We used numerical simulations when drawing the comparison with the empirical results, but included a section which explains a few mathematical aspects of the model and motivates why the numerical simulations were preferred in this case, as well as in the nonlinear extension of the model.

## Empirical methods

Our two fMRI studies (S1 and S2) scanned 96 individuals, ranging emotionally from extremely reactive to extremely nonreactive, and obtained PSSI values for the bilateral ventromedial prefrontal cortex and amygdala. The average-to-reactive range ( $n = 65$ ) was identified using clinical questionnaires (study S1) (Tolkunov et al., 2010), while the average-to-nonreactive range ( $n = 30$ ) was identified using cortisol response in anticipation of a first-time skydive (study S2). A case study ( $n = 1$ ) of exceptional nonreactivity, a bomb squad technician with several military tours of duty defusing explosives during U.S. Navy SEAL missions, used identical methods to the skydive study. This case study has been separated to provide an illustration of the extreme end of the nonreactive spectrum (see Fig. 2 caption). For this manuscript, data from both S1 and S2 were reanalyzed to provide consistency between studies, using the same method for computing the power spectra and a normalized presentation of the PSSI results (fft directly on the BOLD signal), as needed in order to compare them with our model's predictions.

### S1: trait anxiety study

This study was approved by the institutional review board at Stony Brook University; all subjects provided written informed consent. Sixty-five (37 female) healthy adults between the ages of 18 and 49 ( $\mu = 26$ ,  $\sigma = 8$ ) participated in the study. Trait anxiety scores, as measured by the State-Trait Anxiety Inventory for Adults (Mind Garden, Inc., Menlo Park CA), ranged from 21 to 67 ( $\mu = 38$ ,  $\sigma = 10$ ). The fMRI task, a block design using affect-valent (fearful, angry, happy, neutral) facial stimuli, has previously been described (Tolkunov et al., 2010). A lengthy phone screening, as well as the scheduled clinical interview for DSM-IV (Ventura et al., 1998), was administered to rule out subjects with current or prior psychiatric illness. All subjects received a history and a physical; subjects were excluded if they had a history of drug abuse, traumatic brain injury, cardiovascular illness (including high blood pressure), regular nicotine use, or any MRI exclusion criteria, including metal in the body, claustrophobia, or pregnancy/lactation. Subjects were scanned on a 1.5 T Philips Intera MRI scanner at the Stony Brook University Hospital using an 8-channel SENSE parallel head coil. Data were acquired using 136 T2\*-weighted echo planar single-shot images covering the frontal and limbic areas of the brain (oblique coronal) with the following parameters: TR = 2500 ms, SENSE factor = 2, TE = 45 ms, Flip angle = 90°, Matrix dimensions = 256 × 256, FOV = 64 × 64, Slices = 30, Slice-thickness = 4.0 mm, and Gap = 0. The anatomical data were used to generate a customized EPI template to normalize our EPI scans to the standard frame of reference.

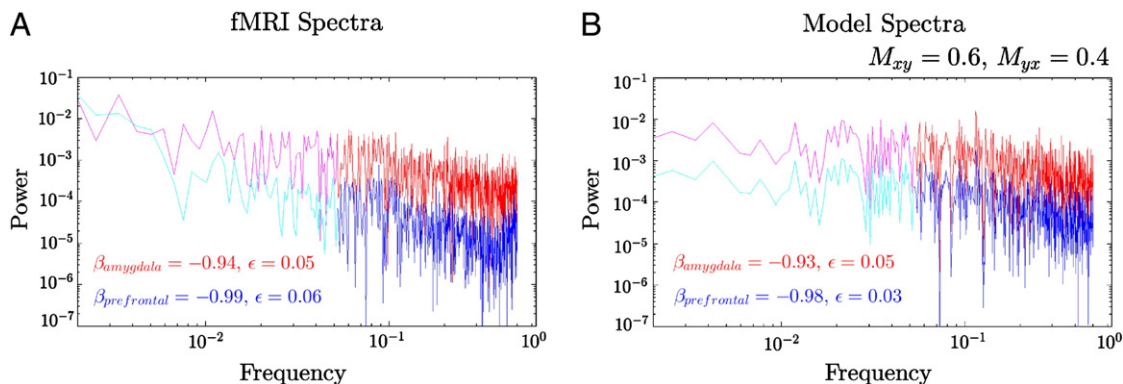


**Fig. 2.** Comparison with data. Amygdala (red) and ventromedial prefrontal (blue) power spectra, A, as seen in the 1090-point long fMRI time series recorded from one of our human subjects, while watching a movie in the scanner, and B, per our model. The axes are logarithmic, but the labels are in physical units. The legends show the region means for the PSSI slopes  $\beta$ , which are comparable. The numerical simulations were performed for a network with  $N = 20$  nodes per module, and time series of length  $L = 100$  and step resolution  $h = 2.5$ . The long-range connectivity densities were fixed to  $M_{xy} = 40\%$  and  $M_{yx} = 50\%$ ; damping coefficients  $\gamma_x = 0.25$ ,  $\gamma_y = 0.25$ , and local connectivity strengths  $g_{xx} = 0.004/N$ ,  $g_{yy} = 0.004/N$ ,  $g_{xy} = 0.2187/N$ ,  $g_{yx} = -0.08/N$ .

The fMRI data analyses were performed using the Statistical Parametric Mapping software (SPM8; <http://www.fil.ion.ucl.ac.uk/spm>), using MATLAB 2010a (Mathworks, Natick MA).

### S2: skydiving study

This study was approved by the institutional review board at Stony Brook University; all subjects provided written informed consent. Thirty (12 female) healthy adults between the ages of 18 and 48 ( $\mu = 24$ ,  $\sigma = 7$ ) participated in the study. Potential participants were screened and demographic/personality measures were acquired in the same manner as S1. Trait anxiety scores ranged from 20 to 53 ( $\mu = 33$ ,  $\sigma = 7$ ). The fMRI task, a block design using countdowns of imminent aversive or benign noise, has previously been described (Carlson et al., 2011). Subjects were scanned on a 3 T Siemens Trio MRI scanner at the Stony Brook University SCAN Center using a 12-channel SENSE parallel head coil. Data were acquired using 232 T2\*-weighted echo planar single-shot images covering the whole brain (oblique coronal) with the following parameters: TR = 2500 ms, SENSE factor = 2, TE = 22 ms, Flip angle = 83°, Matrix dimensions = 96 × 96, FOV = 224 × 224 mm, Slices = 36, Slice thickness = 3.5 mm, and Gap = 0. The anatomical data were used to generate a customized EPI template to normalize our EPI scans to the standard frame of reference. The fMRI data analyses were performed using the Statistical Parametric Mapping software (SPM8; <http://www.fil.ion.ucl.ac.uk/spm>), using MATLAB 2010a (Mathworks, Natick MA).

For Power Spectrum Scale Invariance (PSSI) analyses, we used full raw fMRI BOLD time series, which included all conditions. Using methods previously optimized for fMRI (Rubin et al., 2013), we calculated for each voxel the power spectral density as the squares of the Fourier transformation amplitudes of the linearly detrended time series. To verify that our power spectra indeed obey a power law, we fitted several common shapes to the sample spectra of our longest time series (consisting of 42 min of fMRI data from the left amygdala while the subject engaged on a “guided rest” condition). We fitted the power spectrum (from 0.01 – 0.2 Hz) using a nonlinear least square fit to the following candidate functional profiles: stretched exponential  $Af^{\beta-1}e^{-\lambda f^{\beta}}$ , log-normal  $\frac{1}{\lambda} \exp\left[-\frac{(\ln f - \mu)^2}{2\sigma^2}\right]$  and truncated power law  $Af^{\beta}e^{-\lambda f}$  (including power law  $Af^{\beta}$  for  $\lambda \rightarrow \infty$  and exponential  $Ae^{-\lambda f}$  for  $\beta = 0$ ). While the  $\chi^2$  of the fits were fairly close to each other, only a power law fit produced uniformly distributed residuals while at the same time exhibiting the lowest  $\chi^2$  of all candidate distributions—suggesting a power law as the most appropriate distribution for our data.

From the power spectral density, we computed the scaling parameter by plotting the power spectrum on a log–log scale and estimating the slope by applying a linear fit to the data in the 0.06 – 0.2 Hz range. The upper limit on the frequency range was constrained by the sampling rate, while the lower limit was chosen to avoid confounds due to either task design or physiological variables such as heart rate or respiration (Bär et al., 2007). Being aware that a log–log scale compromises the assumption of Gaussian distribution of errors, we attempted to fit a power law to our data using the Levenberg–Marquardt algorithm. Unfortunately, this algorithm was often unable to converge in an automated fashion, resulting in incomplete data sets. We therefore chose the robust least-square linear fit to the log–log spectra.

## Results

### Numerical simulations

Power spectra show a linear trend in log–log coordinates, over the frequency-band of interest

We considered the log–log power spectra of the simulated time series for each individual node. We used the frequency band

corresponding empirically to 0.025 – 0.2 Hz, an interval which included the frequencies used for computing the PSSI in the experimental time series (Rădulescu et al., 2012; Tolkunov et al., 2010), and which has been previously shown in fMRI to reflect connectivity (Cordes et al., 2001). Over this interval, the spectra were approximately linear: for  $N = 20$ , the average standard error was  $\bar{\epsilon} = 0.08$  (where the average was taken over a  $20 \times 20$  grid of connectivity parameters, ranging from 0% to 100%, and also over  $R = 10$  different runs of the numerical simulation). This is comparable to the goodness of fit obtained in our experimental time series (Rădulescu et al., 2012; Tolkunov et al., 2010). The linearity emerged from tuning the connectivity strengths  $g$  to values within a particular locus; furthermore, the values in this critical locus showed scaling behavior with network size  $N$ .

### $\beta$ is robust within each module and over numerical runs

The model incorporates randomness in two contexts. First, the random input signal was the source of white noise in the system and had a crucial role in driving its behavior in the frequency domain. Second, the inter-module connections were generated randomly for each run of the numerical simulation, according to the preassigned density parameters  $M_{xy}$  and  $M_{yx}$ . While one would expect some level of synchrony of the nodes' activity within each module, one might also expect the values of  $\beta$  to vary widely between runs, driven by the different geometries for the connections within the network nodes. In actuality, however, this did not occur. Even when varying  $M_{xy}$  and  $M_{yx}$  between 0% and 100% of the maximal theoretical value of  $N^2$ , the values of the PSSI slopes  $\beta$  in either module were quite consistent between runs. As shown in Fig. 3, after 100 runs we found that the distributions for each module were normal (almost no outliers), with very small standard deviations  $\sigma_{\text{module}}$  within each module (reflecting the level of synchrony of the nodes within). The standard deviations  $\sigma_{\text{run}}$  of the module-mean  $\beta$ s within each run, although almost one order of magnitude larger than  $\sigma_{\text{module}}$ , were still surprisingly small in comparison with the overall variability of  $\beta$  when allowing different density pairs ( $M_{xy}, M_{yx}$ ).

### $\beta$ varies as a function of both input type (excitatory, inhibitory) and input density

Our simulations showed that when the network was balanced at  $M_{xy} = M_{yx} = 50\%$ , the PSSI for each of the two modules was close to pink noise ( $\beta \sim -1$ ). As the number of excitatory inputs  $M_{xy}$  increased, PSSI of Y shifted towards white ( $\beta = 0$ ) noise. As the number of excitatory inputs  $M_{xy}$  decreased, PSSI of Y shifted towards brown ( $\beta = -2$ ) noise. The opposite was true for inhibitory inputs. As the number of inhibitory inputs  $M_{yx}$  increased, PSSI of X shifted towards brown ( $\beta = -2$ ) noise. As the number of inhibitory inputs  $M_{yx}$  decreased, PSSI of X shifted towards white ( $\beta = 0$ ) noise. Representative examples are shown in Fig. 4.

In Fig. 5, we provide a global representation of PSSI's dependence upon both input type and input density. The surface plots of average PSSI values for both modules were planes, which means that the PSSI values depended linearly on both parameters, changing at different constant rates with respect to each. As expected, both modules in the network were affected by density changes, with the module receiving the altered inputs showing the strongest effects. Also as expected, X and Y were more closely coupled for changes in  $M_{yx}$  as compared to  $M_{xy}$ . This is because our model was designed to receive its exogenous inputs through X (unlike the actual prefrontal-limbic system, which receives parallel exogenous inputs for both regions) and therefore X was dependent upon a greater number of feedback iterations as compared to Y.

### Modeling the hemodynamic response

If applied at a neural scale, the model can be used indirectly in conjunction with blood oxygen level dependent (BOLD) signals produced by fMRI. The latter arise from a coupling between spiking and synaptic

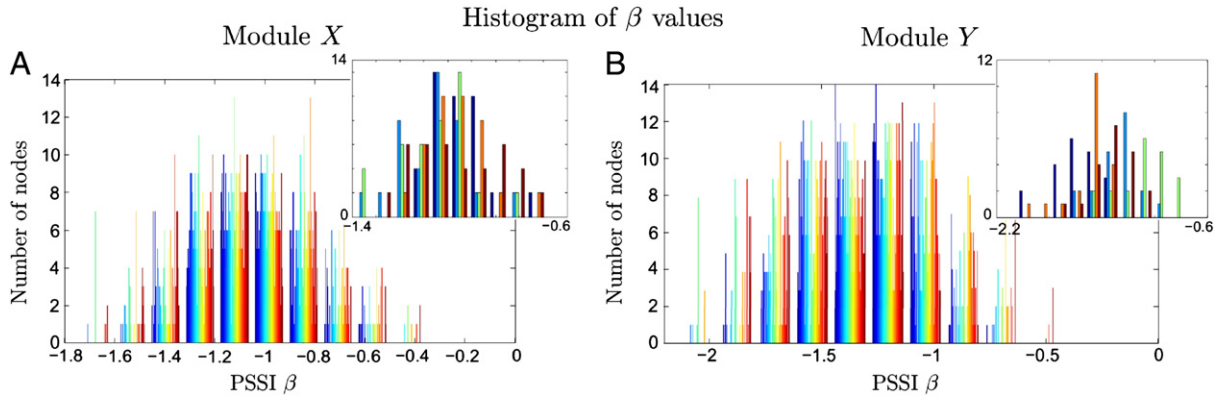


**Fig. 3.** Histogram illustrating model robustness with respect to the random generation of the connectivity graph. The main histograms represent the PSSI slopes  $\beta$  obtained for all the nodes in each module, over  $R = 100$  numeric runs. The inserts show similar illustrations, but in detail for only  $R = 5$  of the 100 runs, in order to clarify the color scheme used: all  $N = 20$  values within each module are shown in the same color for any particular run, so that different runs can be distinguished by different colors. The statistics are described below, with the following notations:  $\mu$  is the mean module-wise  $\beta$  over 100 runs;  $\sigma_{\text{run}}$  is the standard deviation of the module-mean  $\beta$ s, calculated over 100 runs (illustrating the robustness of  $\beta$  between runs);  $\sigma_{\text{module}}$  is the standard deviation of the run-mean  $\beta$ s, over the  $N = 20$  nodes in the module (illustrating the overall level of “synchrony” within each module). A. Module X.  $\mu = -1.06$ ;  $\sigma_{\text{run}} = 0.14$ ,  $\sigma_{\text{module}} = 0.02$ . B. Module Y.  $\mu = -1.30$ ;  $\sigma_{\text{run}} = 0.20$ ,  $\sigma_{\text{module}} = 0.01$ . All simulations were performed for a half-balanced network (long-range connectivity densities  $M_{xy} = 50\%$  and  $M_{yx} = 50\%$ ) with  $N = 20$  nodes per module, with damping coefficients  $\gamma_x = 0.25$ ,  $\gamma_y = 0.25$ , and local connectivity strengths  $g_{xx} = 0.004/N$ ,  $g_{yy} = 0.004/N$ ,  $g_{xy} = 0.21875/N$ ,  $g_{yx} = -0.08/N$ .

activity and the vascular response, with a subsequent change in blood oxygenation. Vascular coupling has been viewed to act either linearly (Li and Freeman, 2007; Logothetis et al., 2001) or nonlinearly (Sheth et al., 2004) on signal amplitudes and frequencies (Freeman and Pasley, 2008; Kellman et al., 2003; Ogawa et al., 2000). In recent years, particular models (e.g., the *balloon model* (Friston et al., 2000), or the *neural mass model* (Logothetis et al., 2001)) have been proposed as reasonable approximations for neurovascular coupling between neural activity and the BOLD response (Rosa et al., 2011). In this section, we use Buxton’s reduced model of the effect of vascular coupling (Buxton et al., 2004), in order to bridge our results to the hemodynamic behavior observed empirically.

In Buxton’s model, with dynamic variables normalized to their baseline values (see Table 1 for the values and significance of parameters), the basic BOLD signal equation is:

$$\frac{\Delta S}{S_0} = A \left( 1 - f^{\alpha_0 - \beta_0} m^{\beta_0} \right), \quad (2)$$

where  $f(t)$  and  $m(t)$  are the cerebral blood flow (CBF) and respectively the cerebral metabolic rate of oxygen (CMRO<sub>2</sub>) responses (normalized to baseline) driven by the underlying neural activity  $N(t)$  (which in our case corresponds to the output signals of the neural model described in the Modeling methods section). The parameters  $\alpha_0$  and  $\beta_0$  (whose values were taken within the empirical ranges shown in Table 1) are respectively the steady-state flow-volume relation and the power law exponent in the relationship  $R \sim \Delta B^{\beta_0}$  between  $R$  (the relaxation rate produced by deoxyhemoglobin in the baseline state) and  $\Delta B$  (the magnitude of field distortions). The model assumes that both CBF and CMRO<sub>2</sub> are linear convolutions of an impulse response function  $h(t)$  with the neural activity  $N(t)$ , so that:

$$f(t) = 1 + (f_1 - 1)h(t - \delta_{t_f}) * N(t) \quad (3)$$

$$m(t) = 1 + (m_1 - 1)h(t - \delta_{t_m}) * N(t), \quad (4)$$

with empirical ranges for the delays  $\delta_{t_f}$  and  $\delta_{t_m}$ , as shown in Table 1. A plausible shape for  $h(t)$  is a gamma-variate function, in this case taken to be on the form:

$$h(t) = \frac{1}{\tau_h k!} \left( \frac{t}{\tau_h} \right)^k e^{-t/\tau_h}, \quad (5)$$

where the parameters  $\tau_h$  and  $k$  are also defined in Table 1. As expected, our simulations found this transformation to act as a low pass frequency filter on our original time series. More precisely, since our neurovascular transformation consists of a convolution with an impulse response function, it left the shape of the spectra unaltered, and only slightly tilted them (increased all  $|\beta|$  by the same constant). Fig. 6A illustrates the slope change for a typical example of time series generated by our model (notice the mean error is the same when performing the linear fitting to the neural versus the hemodynamic log–log spectra, consistently with the fact that the shape of the spectrum is preserved). Fig. 6B illustrates the global variation of the new (hemodynamic) slopes  $\beta$  with respect to the densities  $M_{xy}$  and  $M_{yx}$ , showing that the original results (as seen in Fig. 5) remain qualitatively unchanged through the hemodynamic modulation.

The addition of a neurovascular component is useful in that it permits a more direct comparison between our model and fMRI data. However, it must be considered preliminary due to the fact that convolution acts linearly on the power spectra. Future work will address this aspect in greater detail.

#### Modeling nonlinearity

The original model allowed us to illustrate some basic consequences of the coupled dynamics, while its linear aspect kept the model simple enough to analyze and understand theoretically. However, linearity is implausible in biological systems, and should be only seen as a first order approximation of more realistic behavior, which is most typically nonlinear. In the brain in particular, nonlinear behavior of neurons when processing inputs (Faure and Korn, 2001; Korn and Faure, 2003) has been long supported by data from empirical recordings (Vazquez and Noll, 1998; Xu et al., 2012). A wide variety of formal models have been used to implement nonlinear input integration at the cellular (Hodgkin and Huxley, 1952; Pasemann, 1993), mean-field (Wilson and Cowan, 1972) or macroscopic levels (Friston et al., 2000). While a very accurate biophysical model may consider a membrane-potential approach, and take into account short-scale temporal details (such as recent activation history of each cell), we maintain here (as in the linear model) a mean-field approach, in the tradition of well-known models of excitatory (E) and inhibitory (I) interacting populations (Destexhe and Sejnowski, 2009). The sigmoidal family has been widely proposed as a natural shape to model input integration (Brozović et al., 2008; Marreiros et al., 2008; Wilson and Cowan, 1972), since the actual nonlinear shape of  $E$  and  $I$  responses has not been yet established.

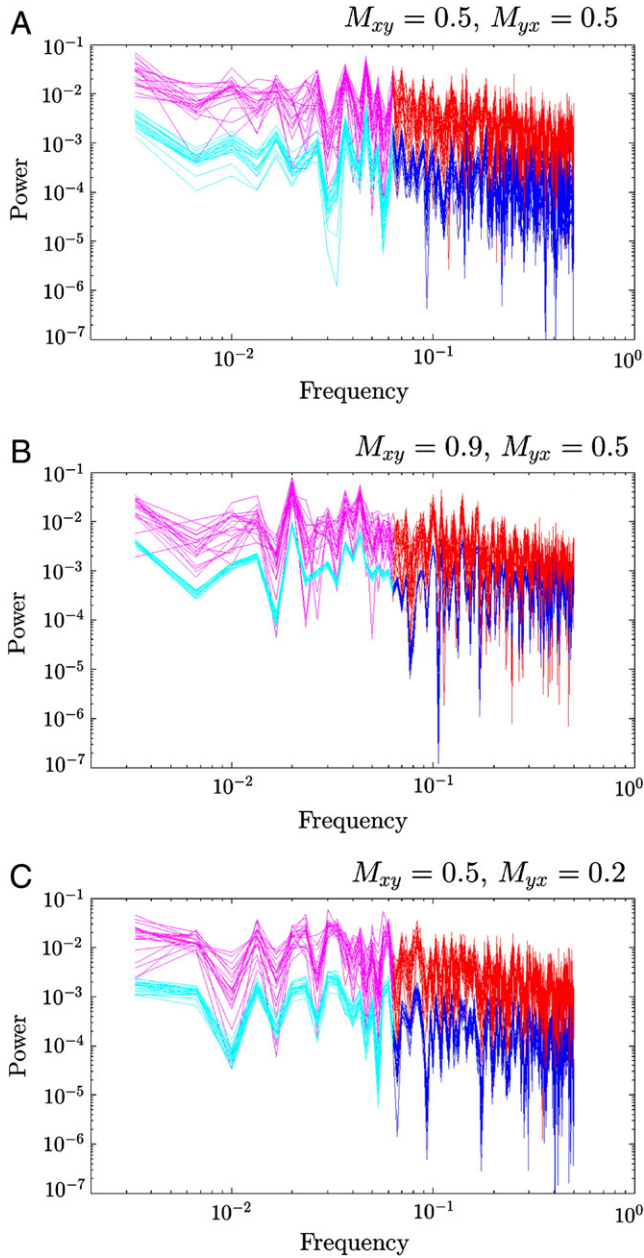


**Fig. 4.** Illustration of PSSI for both modules X and Y as a function of connectivity densities  $M_{xy}$  and  $M_{yx}$  in a network of  $N = 20$  nodes per module. The axes are logarithmic, but the labels are in physical units. Red is used for the excitatory module X, and blue for the inhibitory module Y. For each panel, the text box shows, with the same color coding, the module-mean value of  $\beta$ , the standard deviation  $\sigma$  and the mean goodness of the linear fit ( $\epsilon =$  average standard error). A. For  $M_{xy} = 50\%$ ,  $M_{yx} = 50\%$ ; B. For  $M_{xy} = 90\%$ ,  $M_{yx} = 50\%$ ; C. For  $M_{xy} = 50\%$ ,  $M_{yx} = 20\%$ . All plots illustrate one simulation run, for parameter strengths:  $\gamma_x = 0.25$ ,  $\gamma_y = 0.25$ ,  $g_{xx} = 0.004/N$ ,  $g_{yy} = 0.004/N$ ,  $g_{xy} = 0.21875/N$ , and  $g_{yx} = -0.08/N$ .

Empirically, and probably varies with the type, location and function of the neurons. This way, the neural integrator is set to be most sensitive to input when it falls within a certain magnitude window, and its response will saturate as the sum of inputs becomes unusually strong:

$$S_{b,\theta}(Z) = \frac{1}{1 + \exp(-b[Z-\theta])} - \frac{1}{1 + \exp(b\theta)}. \quad (6)$$

The parameter  $\theta$  modulates the position of the sensitivity window,  $b$  modulates the maximum responsiveness, and  $\tau$  defines the time scale of the response.

In this section, we allow the nodes in our network to act as nonlinear oscillators, and we observe numerically how our results are changed by the nonlinearity. The incoming synaptic input to each node, as described in our original linear model (1), was integrated via a sigmoidal function. The nonlinear system describing the evolution of  $x_k$  and  $y_k$ , for  $k = 1, \dots, N$  is then:

$$\begin{aligned} \frac{dx_k}{dt} &= S_{b_e, \theta_e} \left( -\gamma_x x_k + \sum_{p=1}^N g_{yx} A_{kp} (y_p - x_k) + \sum_{p=1}^N g_{xx} (x_p - x_k) \right) + I_k(t) \\ \frac{dy_k}{dt} &= S_{b_i, \theta_i} \left( -\gamma_y y_k + \sum_{p=1}^N g_{xy} B_{kp} (x_p - y_k) + \sum_{p=1}^N g_{yy} (y_p - y_k) \right), \end{aligned} \quad (7)$$

where  $S_{b_e, \theta_e}$  and  $S_{b_i, \theta_i}$  are E and I sigmoidal functions, defined as in Eq. (6). The sigmoidal parameters  $(b_e, \theta_e)$  and  $(b_i, \theta_i)$  respectively, were chosen within the range used for the corresponding parameters in the original Wilson–Cowan model (Wilson and Cowan, 1972), as well as in subsequent related work (Borisjuk et al., 1995) (see Figs. 7 and 8 captions).

In order to increase the model’s realism, the strengths  $\bar{g}_{xx}(k, p)$  of the connections between  $x_k$  and  $x_p$  were defined to be normally distributed around the mean  $g_{xx}$  (the original value of the identical connection strength); similarly, we defined normal distributions for  $\bar{g}_{yx}(k, p)$ ,  $\bar{g}_{xy}(k, p)$  and  $\bar{g}_{yy}(k, p)$ .

A first glance at the spectra of the nonlinear extension reveals a much wider power law window. In Fig. 7B, we compare, for a typical spectrum using the nonlinear model, the log–log linear fit on the narrower 0.025 – 0.2 Hz frequency band to the linear fit on the wider band 0.001 – 0.2 Hz (corresponding to the whole log–log spectrum, except the first point). Fig. 7A, shows the comparable slope values for both frequency bands, in the case of the linear model, illustrating clearly how much better the nonlinear model behaves with respect to PSSI. It is, of course, not a surprise that the nonlinear extension provides a better estimation of real neural behavior, where power law of the spectra has been consistently observed to encompass the low frequency range as well (Achard et al., 2006; Ciucu et al., 2012; He, 2011; Zarahn et al., 1997).

When re-performing the numerical computations of the spectra for the nonlinear model, we found the spectra to be quantitatively steeper (Fig. 7), although the slopes remained broadly within the range  $[-2, 0]$ . However, the changes in the slopes when varying  $M_{xy}$  and  $M_{yx}$  were preserved qualitatively, and were consistent even when using the larger band-width 0.001 – 0.2 Hz (as illustrated in Fig. 8).

### Empirical results

As shown in Fig. 9, individuals who were in the middle range of the spectrum had  $\beta$  values in the pink noise range, for both the amygdala (excitatory) and prefrontal (inhibitory) areas. Individuals who were more fearful showed limbic  $\beta$  values closer to zero, but localized to the amygdala (Tolkunov et al., 2010). Individuals who were more fearless also showed limbic  $\beta$  values closer to zero, but localized to the prefrontal cortex.

### Analytical considerations for the linear model

Our system

$$\dot{X}(t) = CX(t) + J(t) \quad (8)$$

is a stochastic relaxation process, where  $J(t)$  is the input noise vector (Wiener process). The behavior of such (Ornstein–Uhlenbeck (OU) (Bibbona et al., 2008; Ricciardi and Sacerdote, 1979)) stochastic processes is fairly well understood, being driven by the nature of the input noise overposed on the system’s deterministic aspect (which is linear). The dynamics of the one-dimensional OU is quite easy to

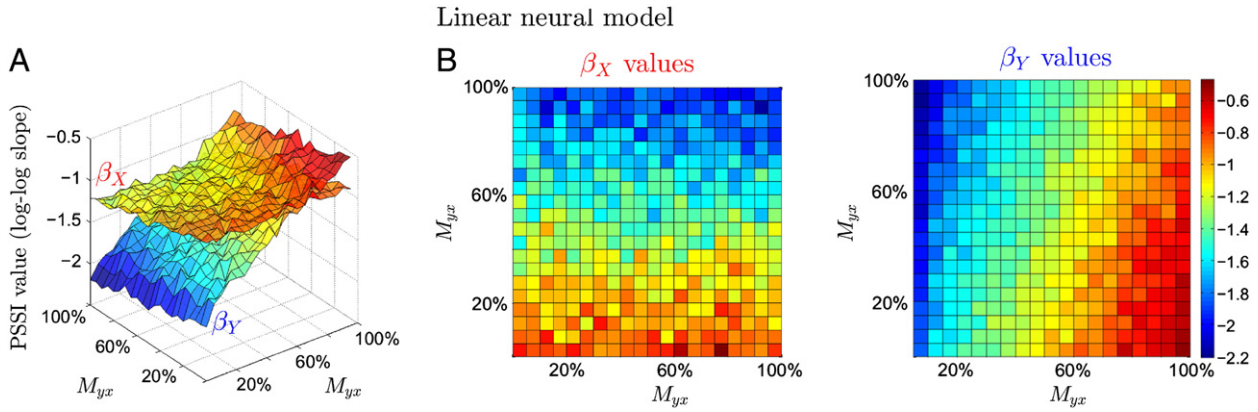


**Fig. 5.** PSSI shifts as a function of input control and input density. A. Dependence of scale invariant slopes  $\beta$  on the excitatory and inhibitory connectivity densities, as per our model simulations, shown as surface functions of  $M_{xy}$  and  $M_{yx}$ . B. Same illustration in which the two surfaces  $\beta_X$  (left) and  $\beta_Y$  (right) are shown as pcolor plots. The simulations were performed for the following parameter values:  $N = 20$ ,  $\gamma_x = 0.25$ ,  $\gamma_y = 0.25$ ,  $g_{xx} = 0.004/N$ ,  $g_{yy} = 0.004/N$ ,  $g_{xy} = 0.21875/N$ ,  $g_{yx} = -0.08/N$ . The plane best approximating the surface for  $\beta_X$  (excitatory) has negative slope  $-0.0008$  in the direction of increasing  $M_{xy}$ , and negative slope  $-0.02$  in the direction of increasing  $M_{yx}$ ; the plane best approximating the surface for  $\beta_Y$  (inhibitory) has positive slope  $0.06$  in the direction of increasing  $M_{xy}$ , and negative slope  $-0.02$  in the direction of increasing  $M_{yx}$ .

determine for given parameters, and in a multi-variate context it is dictated by the spectrum of the Jacobian matrix. In our case, this matrix, which captures the system's "connectivity," depends simultaneously not only on eight parameters (on the damping coefficients  $\gamma_x$  and  $\gamma_y$ , on the short-range and inter-modular connectivity strengths  $g_{xx}$ ,  $g_{yy}$  and  $g_{xy}$ ,  $g_{yx}$ , respectively, and on the inter-modular connection density parameters  $M_{xy}$  and  $M_{yx}$ ) but also on a random aspect (the geometry of the connections). It is the structure of this random matrix that complicates in our case a direct and rigorous sensitivity analysis, and relegated us to numerical approaches (Kloeden et al., 1994). Below we make some conjectures about the behavior of the eigenvalues, and about their impact on the dynamics. A more extensive analytical approach, while not within the scope of this paper, is the object of our current work (see Discussion section).

An important, and rather surprising, feature of the simulations was that the dynamic results were extremely robust between numerical runs. This is due to the fact that, when fixing all system parameters (damping, connectivity strengths and densities), the eigenvalues of the Jacobian matrix do not vary substantially with the edge geometry. This is not a parameter-dependent artificial property, but rather a more intrinsic feature of the underlying graph. It is the robustness of the network architecture (as encoded by its adjacency matrix) that reflects into the robustness of the temporal systemic dynamics (as captured by the power spectra of the node trajectories).

**Table 1**  
Parameters for the neural-vascular model. The range of each parameter is given per Buxton et al. (2004). The value for each parameter is the value used in our simulations.

Name	Empirical range	Value	Units	Description
$\alpha_0$	0.4	0.4	–	Steady-state flow volume
$\beta_0$	1–2	1.5	–	Relationship between $R \sim \Delta B^{\beta_0}$
$f_1$	1–2	2	–	Amplitude of CMRO2 response to neural activation
$n = \frac{f_1 - 1}{m_1 - 1}$	2–3	2	–	Steady-state flow-metabolism relation
$m_1$	–	0.4	–	Amplitude of CMRO2 response to neural activation
$\delta_{t_f}$	–	2	s	Delay between stimulus and CBF
$\delta_{t_m}$	–	3	s	Delay between stimulus and CMRO2
$\delta_t = \delta_{t_m} - \delta_{t_f}$	0–2	1	s	Delay between CBF and CMRO2
$\tau_h$	~1	0.4	s	–
$k$	3	3	–	–
$A$	0.075	–	–	Maximum BOLD signal change

#### Adjacency properties, network geometry and the Jacobian matrix

Rather than working with the densities  $M_{xy}$  and  $M_{yx}$ , it is more convenient in this section to simply refer to the numbers of oriented edges from nodes in  $X$  to nodes in  $Y$  (which we called  $\alpha$ ), and from nodes in  $Y$  to nodes in  $X$  (which we called  $\delta$ ). In other words, in terms of the edge density parameters,  $\alpha = M_{xy}N^2$  and  $\delta = M_{yx}N^2$ .

The adjacency matrix of our graph is of the form:  $t = \begin{bmatrix} M & A \\ B & M \end{bmatrix}$ , where  $M$  is the  $N \times N$  matrix with all entries equal to 1, the block  $A$  has  $\alpha$  entries equal to one, and the block  $B$  has  $\delta$  entries equal to one. For fixed  $0 \leq \alpha, \delta \leq N^2$ , if we call  $\mathcal{D}^{\alpha, \delta}$  the distribution of  $2N \times 2N$  adjacency matrices  $T$  with  $\alpha$  ones in block  $A$  and  $\delta$  ones in block  $B$ , then clearly the cardinality

$$|\mathcal{D}^{\alpha, \delta}| = \binom{\alpha}{N^2} \binom{\delta}{N^2}. \quad (9)$$

While in general one would expect the eigenvalues of  $T$  to depend strongly on the actual exact positions of the 1's within the blocks  $A$  and  $B$ , we have noticed that each eigenvalue  $\lambda_j(T)$  varies, for  $T \in \mathcal{D}^{\alpha, \delta}$ , within a very narrow distribution  $\mathcal{L}_j^{\alpha, \delta}$ . We conjecture the following:

**Conjecture.** The expected values of  $\lambda_j$  are approximately:  $\langle \lambda_1 \rangle \cong N + \frac{\sqrt{\alpha\delta}}{N}$ ,  $\langle \lambda_2 \rangle \cong N - \frac{\sqrt{\alpha\delta}}{N}$ , and  $\langle \lambda_3 \rangle, \dots, \langle \lambda_{2N} \rangle \cong 0$  (with multiplicity  $2N - 2$ ). Moreover, the variance of each  $\mathcal{L}_j^{\alpha, \delta}$  decreases with  $N$ , even though the cardinality of each  $\mathcal{D}^{\alpha, \delta}$  increases factorially with  $N$ .

While a formal proof is beyond the scope of this paper, and the general case remains an open question, we have investigated three different directions that support this conjecture. First, the adjacency matrix  $T$  is a

block matrix with  $2 \times 2$  weighted density matrix  $D = \begin{bmatrix} 1 & \frac{\alpha}{N^2} \\ \frac{\delta}{N^2} & 1 \end{bmatrix} =$

$\begin{bmatrix} 1 & M_{xy} \\ M_{yx} & 1 \end{bmatrix}$ . According to a result of Juhász (1990),  $T$  has two eigenvalues that are large in absolute value (of order  $N$ ), with:  $\langle \lambda_{1,2} \rangle = N \pm \frac{\sqrt{\alpha\delta}}{N} + o(N^{1/2+\epsilon})$  in probability, for any  $\epsilon > 0$ , while the other eigenvalues are of order  $o(N^{1/2+\epsilon})$  in probability, for any  $\epsilon > 0$ . Juhász' paper does not provide, however, exact formulae for the expected eigenvalues, and it does not show that their distributions narrow with increasing  $N$ .

Second, we calculated exactly the expected values and variances for  $N \leq 5$ , and numerically approximated them for larger  $N$ s, using a sample of 100 possible  $T$ s (since  $\mathcal{D}^{\alpha, \delta}$  becomes too large to inspect entirely). We have obtained sample-based mean and variances for the real parts

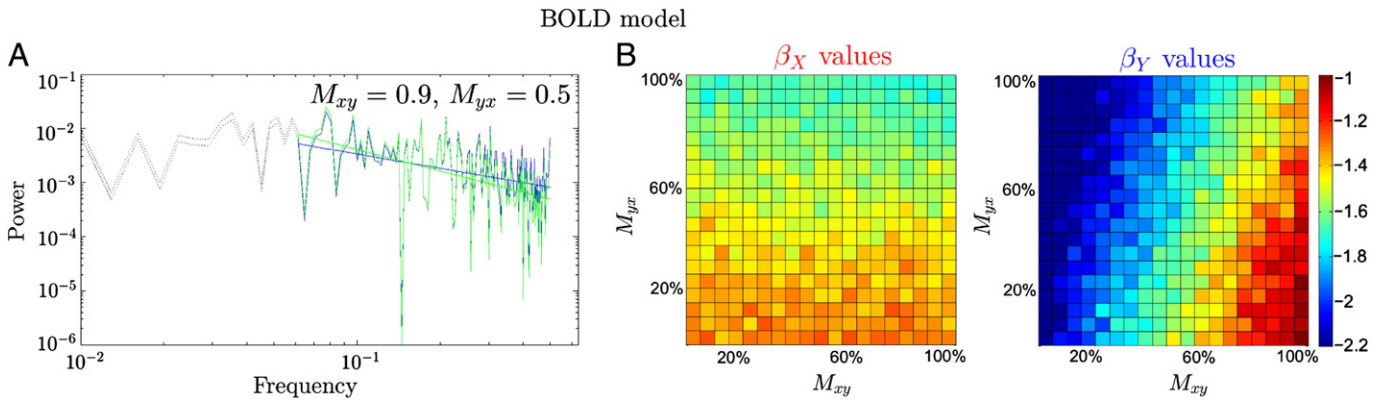


**Fig. 6.** Linear fitting and PSSI for the hemodynamic time series. A. The convolution with the hemodynamic finite impulse response function acts on the solutions of our model as a low pass frequency filter. The shape of the frequency profile is preserved, with comparable goodness of fit when fitting a line to the log–log spectrum. The slope of this linear fit is more negative (spectrum is slightly steeper) after the hemodynamic transformation, although the new values of  $\beta$  remain within the white noise to brown noise range. B. PSSI shifts as a function of densities, for the BOLD model time series. The surfaces  $\beta_X$  (left) and  $\beta_Y$  (right) are shown as pcolor plots. The two surfaces were obtained in parallel with the corresponding ones in Fig. 5. Notice that the hemodynamic modulation has shifted the two surfaces by a negative constant, while maintaining the values in the overall  $[-2,0]$  range.

of all eigenvalues of  $T$ . In Fig. 10A we represented these means as surface-functions depending of the density parameters  $M_{xy} = ha/N^2$  and  $M_{yx} = \delta/N^2$ ; the corresponding approximations match the Juhász surfaces very closely.

Third, we were able to rigorously check the conjectured formula for the particular case in which one of the densities is 1 (i.e., either  $\alpha = N^2$  or  $\delta = N^2$ ), and show that in this case the variance is zero (i.e., the eigenvalues are completely independent on the geometry of the connections in the remaining random block).

Finally, it is important to note that this robustness of the eigenvalues in the adjacency spectrum is not simply due to the full connectedness of the modules  $X$  and  $Y$  (the  $M$  corners of the adjacency matrix  $T$ ). The result persists when pruning 1 s randomly out of these corners, and breaks down only when all connections have been removed. This is a valuable property when determining which connectivity schemes are safe to use for models of learning, or other cognitive algorithms in theoretical neuroscience. Popular biophysically plausible choices range from considering fully-connected to fully-disconnected interacting networks, or layers (O’Reilly and Frank, 2006). In our modeling framework, learning is not a priori prevented in any of these schemes.

The Jacobian (connectivity) matrix of our OU system is given in block form by:

$$C = \begin{bmatrix} C_{xx} & C_{yx} \\ C_{xy} & C_{yy} \end{bmatrix}, \tag{10}$$

where the four  $N \times N$  blocks are  $C_{xx} = -(\gamma_x + Ng_{xx})I - g_{yx}D_A + g_{xx}M$ ,  $C_{yx} = A^T g_{yx}$ ,  $C_{xy} = B^T g_{xy}$ ,  $C_{yy} = -(\gamma_y + Ng_{yy})I - g_{xy}D_B + g_{yy}M$  (here we used the notation  $D_A$  for the diagonal matrix with entries the sum of elements of each column of  $A$ , and the same for  $D_B$ ).

For the ensemble of parameters used, all eigenvalues of the Jacobian have a negative real part, so that the system is asymptotically stable (has a stationary solution). The analytical dependence of the eigenvalues upon these parameters is complicated in the general case; we were able to calculate the characteristic polynomial in the particular case of one maximal density, and proved (in this case) that its coefficients do not change when rescaling  $g$  as  $1/N$ , thus explaining the scaling behavior of the system with network size.

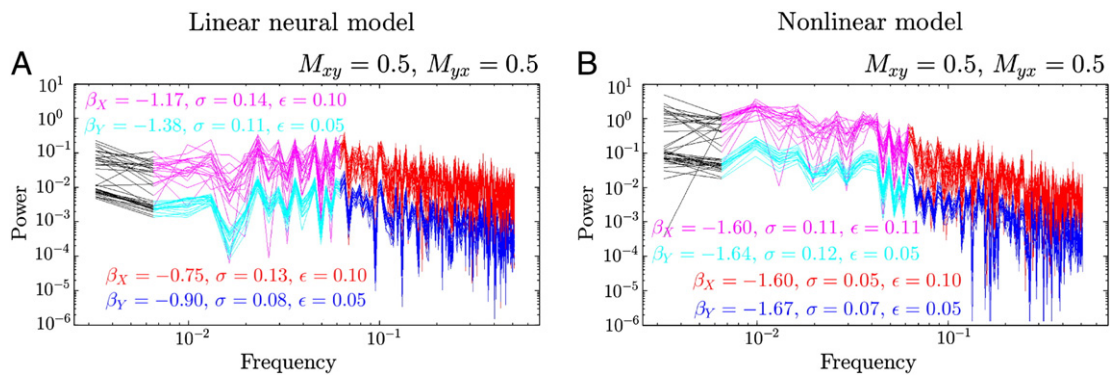


**Fig. 7.** Comparison of PSSI between the linear model and the nonlinear extension, illustrated by an example of the respective spectra in  $X$  and  $Y$ , for  $M_{xy} = M_{yx} = 0.5$ . The axes are logarithmic, but the labels are in physical units. The slopes of the best linear fit to the log–log spectra are calculated for two band widths: 0.025 – 0.2 Hz, and 0.001 – 0.2 Hz (i.e., the whole spectrum, except the first point). The spectra and the corresponding slope statistics are shown for module  $X$  in red (for 0.025 – 0.2 Hz) and in magenta (for 0.001 – 0.2 Hz), and for module  $Y$  in blue (for 0.025 – 0.2 Hz) and in cyan (for 0.025 – 0.2 Hz). The two panels represent the linear model (A) and the nonlinear model (B). In the nonlinear case, the slopes are almost identical between the two band widths, indicating a much wider range PSSI behavior in the nonlinear model, when compared to its linear counterpart. Compare the shapes of the spectra in B with those of the empirical spectra in Fig. 2A. Parameter values:  $N = 20$ ,  $\gamma_x = 0.25$ ,  $\gamma_y = 0.25$ , and  $\bar{g}_{xx}$ ,  $\bar{g}_{yy}$ ,  $\bar{g}_{xy}$  and  $\bar{g}_{yx}$  drawn out of normal distributions with means  $g_{xx} = 0.004/N$ ,  $g_{yy} = 0.004/N$ ,  $g_{xy} = 0.21875/N$ ,  $g_{yx} = -0.08/N$  and standard deviation  $0.001/N$ . The sigmoidal parameters were fixed to:  $b_e = 1.6$ ,  $\theta_e = 4$ ,  $b_i = 1.3$ ,  $\theta_i = 3.7$ ,  $\tau = 0.01$ .

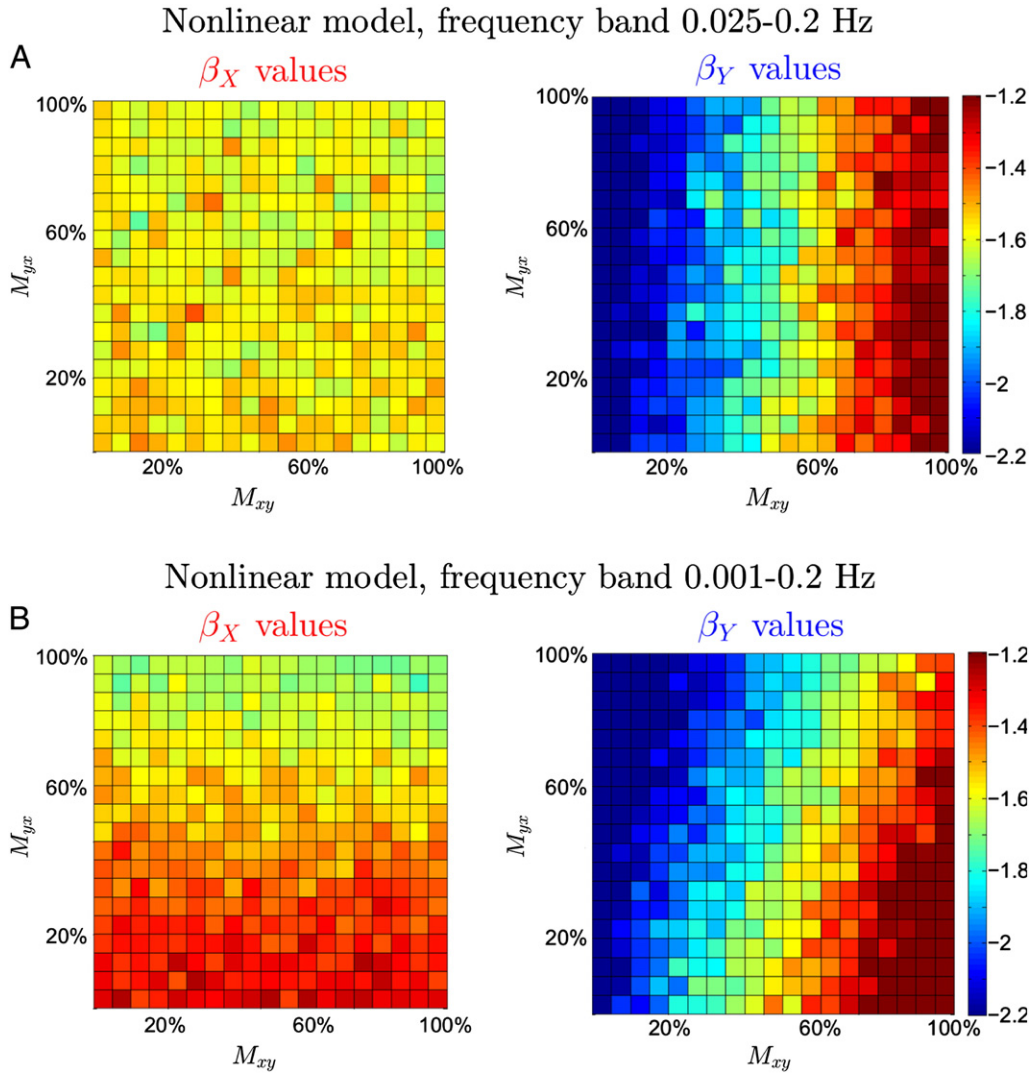


**Fig. 8.** Comparison of the log-log slopes in the nonlinear model, for linear fitting performed to two different frequency bands of the power spectra. The dependence of the slopes  $\beta_x$  (left) and  $\beta_y$  (right) on the densities  $M_{xy}$  and  $M_{yx}$  is illustrated as pcolor plots, for the frequency interval 0.025 – 0.2 Hz (A.) and 0.001 – 0.2 Hz (B.). The changes in the slopes in response to variations in the pair  $(M_{xy}, M_{yx})$  are qualitatively consistent between the two panels. The numerical computations were performed for  $N = 20$ , with each slope averaged over  $R = 10$  numerical runs, for parameter values:  $\gamma_x = 0.25$ ,  $\gamma_y = 0.25$ , and  $\bar{g}_{xx}$ ,  $\bar{g}_{yy}$ ,  $\bar{g}_{xy}$  and  $\bar{g}_{yx}$  drawn out of normal distributions with means  $g_{xx} = 0.004/N$ ,  $g_{yy} = 0.004/N$ ,  $g_{xy} = 0.21875/N$ ,  $g_{yx} = -0.08/N$  and standard deviation  $0.001/N$ . The sigmoidal parameters were fixed to:  $b_e = 1.6$ ,  $\theta_e = 4$ ,  $b_i = 1.3$ ,  $\theta_i = 3.7$ ,  $\tau = 0.01$ .

### The power spectrum

OU processes are well known to have Lorentzian power spectra (Mitra and Bokil, 2007), often referred to as *red noise* (Monahan, 1998). Their correlation function decays at long times, so that the power spectrum, which is the Fourier transform of the correlation function, also decreases monotonically with the frequency. More precisely: for frequencies  $f \ll 1$ , the power spectrum is a constant (i.e.,  $\beta = 0$ , white noise); on the other hand, for large  $f$ , the spectrum becomes proportional with  $1/f^2$  (i.e.,  $\beta = 2$ , brown noise).

For our OU system (8) in particular, the continuous power spectra for solutions  $X = (x_1, \dots, x_N, y_1, \dots, y_N)^T$  on a compact interval  $[0, T]$  can be calculated by taking the continuous Fourier transform  $\tilde{X}_c$ , so that the power for any real frequency  $w$  can be calculated from:

$$\left[ \frac{2\pi}{T} iwI - C \right] \tilde{X}_c(w) = \tilde{J}(w) - \frac{\Delta X}{T}, \quad (11)$$

where  $\Delta X = X(T) - X(0)$ . This produces, as explained above, two pieces, each with almost constant slope (depending on the parameter values), connected by a smooth elbow (see Fig. 11). Moreover, changes

in the density parameters  $M_{xy}$  and  $M_{yx}$  trigger qualitative changes in the spectra (e.g., position of the elbow, slope of each piece). The analytical dependence of the power spectrum properties on the density parameters is not trivial to express for the general case. We present below, as illustration, a simple application in which the computations can be carried out explicitly for the special case of only two nodes  $x$  and  $y$  ( $N = 1$ ), and thus only one possible geometry. The system then becomes:

$$\begin{aligned} \frac{dx}{dt} &= -\gamma_x x + g_{yx}(y-x) + j(t) = -(\gamma_x + g_{yx})x + g_{yx}y + j(t) \\ \frac{dy}{dt} &= -\gamma_y y + g_{xy}(x-y) = -(\gamma_y + g_{xy})y + g_{xy}x. \end{aligned} \quad (12)$$

The calculation of the Fourier transform for  $x$  and  $y$  is straightforward. For example:

$$\tilde{y} = \frac{\epsilon g_{xy}}{\left[ iw + (\gamma_x + g_{yx}) \right] \left[ iw + (\gamma_y + g_{xy}) \right] - g_{xy}g_{yx}}, \quad (13)$$

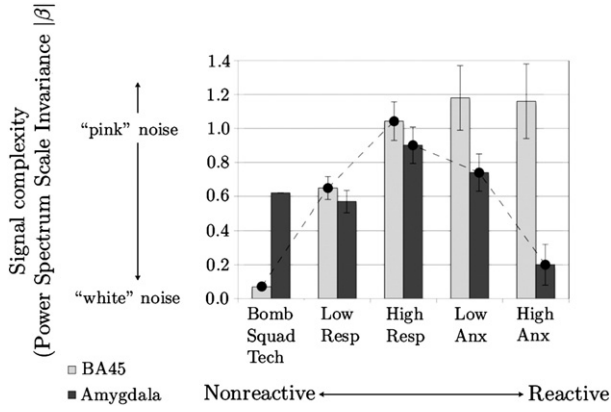


**Fig. 9.** PSSI shifts as observed in the amygdala and ventromedial prefrontal cortex (Brodmann Area 45), for 96 adults ranging from nonreactive to highly reactive. To graphically demonstrate results over the entire spectrum, we used a  $k$ -means cluster analysis ( $k = 3$ , discarding middle group) to classify subjects from two independent cohorts. For the more reactive end of the spectrum, subjects were separated into highest (51.17,  $n = 12$ ) and lowest (27.63,  $n = 16$ ) trait anxiety. For the less reactive end of the spectrum, subjects were separated into those who showed greatest (“high-responder”: 26.62 nmol/l,  $n = 5$ ) and least (“low-responder”: 0.99 nmol/l,  $n = 14$ ) cortisol increases to a first-time tandem skydive. To pin the least reactive end of the spectrum, as part of the same study we also obtained data from a single bomb squad technician. Individuals in the middle range of the reactivity spectrum had PSSI values in the pink noise range, for both the amygdala and BA45. Both extreme ends of the spectrum showed prefrontal-limbic PSSI values closer to zero: localized to the amygdala for more reactive individuals, and to BA45 for less reactive individuals.

where  $\epsilon = \tilde{j}(w)$ . From the Fourier transform, the transfer function of  $y$  is, in polar form:

$$\rho = \frac{1}{2K} \left[ \cos(\theta) \pm \sqrt{\cos^2(\theta) + \frac{4K}{Q^2} \sin^2(\theta)} \right], \quad (14)$$

where  $Q = -(\gamma_x + \gamma_y) - (g_{xy} + g_{yx})$  and  $K = (\gamma_x + g_{yx})(\gamma_y + g_{xy}) - g_{xy}g_{yx}$ . For parameters within our functional range, this is a generalized limaçon, whose geometric characteristics, dependent on the densities, are thus usable as markers of the connectivity profile (see Fig. 12 for an illustration of the limaçons for two different system densities). The power spectrum will be given by:

$$\|\tilde{y}\|^2 = \frac{\epsilon^2 g_{xy}^2}{w^4 + (Q^2 - 2K)w^2 + K}, \quad (15)$$

or, in log–log form  $f \rightarrow P(f)$ , with  $P = \log(\|\tilde{y}\|^2)$  and  $f = \log(w)$ :

$$P(f) = 2 \log(\epsilon g_{xy}) - \log\left(e^{4f} + (Q^2 - 2K)e^{2f} + K\right). \quad (16)$$

This illustrates, in this special case, the general shape of the log–log spectra discussed above: a two-segment almost piecewise linear function. For small values of  $w > 0$ , the constant term dominates in the denominator of Eq. (15), so that the log–log spectral slope  $\beta \sim 0$ ; for large values of  $w$ ,  $w^4$  dominates in the denominator, so that the power spectrum is approximately  $\epsilon^2 g_{xy}^2 w^{-4}$ , and the log–log slope  $\beta \sim -4$ ; for a short interval of intermediary frequencies  $w$ , the middle term has a comparable impact, and produces the elbow with variable log–log slope  $\beta$ .

In order to facilitate comparison with signals measured empirically (which are discrete), we analyzed discrete spectra (for length  $L = 300$ , and time resolution  $h = 2.5$  used in our numerical simulations in conjunction with the Euler–Maruyama numerical solver). The discrete Fourier transform  $\tilde{X}(k)$  can be expressed, for  $0 \leq k \leq L$ , as:

$$\left[ \frac{a_k}{h} I - C \right] \tilde{X}(k) = \tilde{J}(k) - \frac{(a_k + 1)\Delta X}{T}, \quad (17)$$

where  $T = hL$ ,  $a_k = e^{2\pi i k/L} - 1$  and  $\Delta X = X(T) - X(0)$ .

Clearly, neither the continuous-time, nor the discrete PSDs, follow power laws when considered over the whole frequency range. So why are we authorized to perform a linear fitting to the analytical discrete spectra, and compare their slopes with the empirical slopes? While in general there are (particularly low and high frequency) distortions due to the discretization process, for connectivity strengths  $g$  within our critical range, the shape of the discrete spectra is comparable qualitatively with that of the continuous spectra: two approximately linear pieces, connected by a round elbow. Our simulations have been restricted to the frequency band 0.025 – 0.2 Hz, included within the second linear piece, for all parameter values. In addition, this band encompasses the frequency range for which PSSI was obtained empirically (0.06 – 0.2 Hz, known from literature to be most reflective of connectivity). Notice that the discrete spectra tail off at the high frequency end. This is also a well-known feature of empirical imaging spectra (as seen for example in Fig. 2A, and also in (Lai et al., 2010)), and in our case does not significantly alter the overall slope of the second almost linear piece, from the turn of the elbow to the end (see Fig. 11A, or Fig. 11B for an alternative illustration of the shape of the spectra using derivatives).

Finally, let us comment on a robustness property: the changes triggered in slope by changes in the density parameters  $M_{xy}$  and  $M_{yx}$  appear to be qualitatively consistent between the continuous and the discrete spectra. This is important, since it allows our theoretical-to-empirical model translation to be independent on the length and resolution of

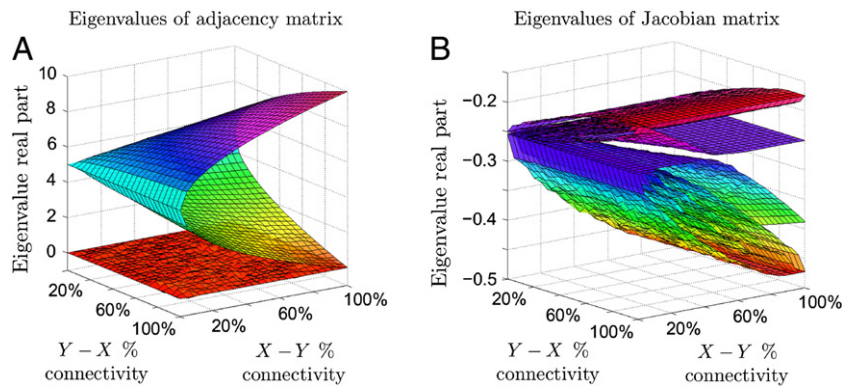


**Fig. 10.** Spectral matrix representations. Surface plot of A. the real part of the adjacency matrix eigenvalues and B. the eigenvalues of the Jacobian of the system, both with respect to  $M_{xy}$  (along the x-axis) and  $M_{yx}$  (along the y-axis), and averaged over a sample of 20 adjacency configurations. Eigenvalues are relatively robust under different adjacency schemes, as long as the connectivity densities are fixed. The illustration was performed for the following parameter values:  $N = 5$ ,  $\gamma_x = 0.25$ ,  $\gamma_y = 0.25$ ,  $g_{xx} = 0.004/N$ ,  $g_{yy} = 0.004/N$ ,  $g_{xy} = 0.21875/N$ ,  $g_{yx} = -0.08/N$ .

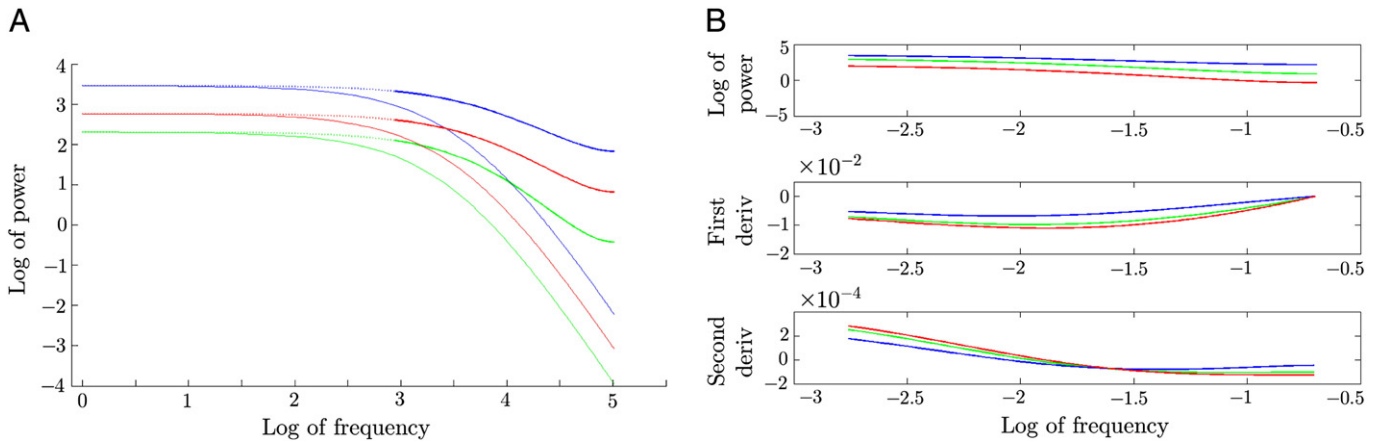


**Fig. 11.** Analytical power-spectra. A. The spectra of a Y node for, respectively,  $M_{xy} = 0.9, M_{yx} = 0.5$  (blue curves);  $M_{xy} = 0.5, M_{yx} = 0.5$  (red curves);  $M_{xy} = 0.2, M_{yx} = 0.5$  (green curves). The thick curves represent discrete spectra for time resolution  $h = 2.5$  and length  $L = 300$  data points (consistent with our numerical results), with the solid line marking the frequency band width for which the fitting was performed in the numerical simulations with noise. The thin curves represent continuous spectra. All plots were based on formal computations (see the Analytical considerations for the linear model section) rather than on numerically solving the system. Notice that changes in the densities  $M_{xy}$  and  $M_{yx}$  produce the same qualitative changes in shape between the corresponding discrete and continuous spectra. B. Formal power spectrum of a Y node (top), its derivative (middle) and its second derivative (bottom), for  $M_{xy} = 0.9, M_{yx} = 0.5$  (blue curves),  $M_{xy} = 0.5, M_{yx} = 0.5$  (red curves) and  $M_{xy} = 0.2, M_{yx} = 0.5$  (green curves), respectively. Notice that the second derivatives remain very close to zero within our frequency band (their variation is 2 orders of magnitude smaller than the variation in the first derivative, and 4 orders of magnitude smaller than the variation in the original log power spectrum), supporting our assumption of almost linearity of the spectra within this frequency range. All illustrations were performed, for consistency with the numerical results, with the following parameter values:  $N = 20, \gamma_x = 0.25, \gamma_y = 0.25, g_{xx} = 0.004/N, g_{yy} = 0.004/N, g_{xy} = 0.21875/N,$  and  $g_{yx} = -0.08/N$ .

the time series, as long as these are consistent between model and experiment.

**Discussion**

Our model shows that, for sufficiently large networks, PSSI can be obtained within certain frequency bands in a context as simple as a linear stochastic system of differential equations, although more subtle nonlinear dynamics can greatly widen the frequency band of PSSI, and improve the system’s performance. Our model further demonstrates that  $\beta$  values vary as a function of both input type (excitatory, inhibitory) and input density (mean number of long-range connections), independent of their node-specific geometric distribution.

Our simulation results suggest a testable framework for interpreting empirical data. In our data set, individuals with average emotional reactivity (who have PSSI values in the pink noise range for both amygdala and prefrontal regions) should have well-regulated control systems, in which excitatory and inhibitory influences are balanced. Individuals at the more reactive (anxious) end of the spectrum, showing white noise primarily for the amygdala, should have relatively weaker inhibitory

inputs from the prefrontal cortex (producing weaker feedback). Individuals at the less reactive end of the spectrum, showing white noise primarily for the prefrontal cortex, should have relatively stronger excitatory inputs from the amygdala (producing stronger feedback). This last simulation result may seem surprising, but in fact produces a reasonable hypothesis: enhanced projections from the amygdala to the prefrontal cortex effectively lower the threshold for inhibitory feedback, thereby suppressing all but the strongest stimuli. Functional and structural connectivity techniques, such as dynamic causal modeling (Friston et al., 2003; Stephan et al., 2007) and diffusion tensor imaging (Iturria-Medina et al., 2008), are ideally suited towards empirically testing these hypotheses.

*Specific modeling remarks*

Our simulations suggest that a global parameter sensitivity analysis of the system might reveal that linearity of spectra over the connectivity frequency range (as found by our numerical simulations as well as empirically) is restricted to a critical locus in the parameter space. This hypothesis is supported by the fact that the fine tuning of the connectivity

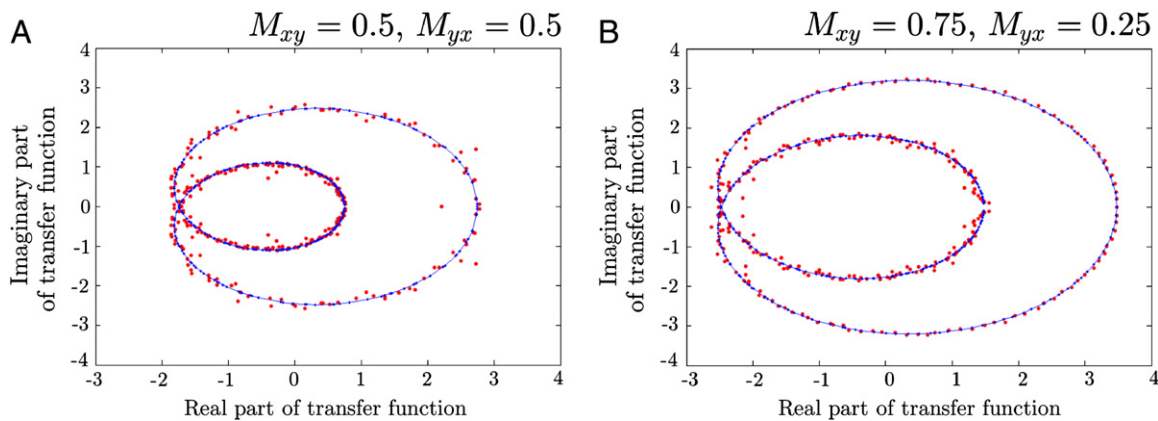


**Fig. 12.** Polar plot of the transfer functions corresponding to the nodes in Y, for A.  $M_{xy} = 50\%, \beta = 50\%$ ; B.  $M_{xy} = 75\%, M_{yx} = 25\%$ . Perturbations in the connectivity profile ( $M_{xy}; M_{yx}$ ) of the network, shown to reflect into changes in the log–log spectral slopes  $\beta$ , can be alternatively captured, quantitatively and visually, as changes in the geometric properties (e.g., curvature, area of the inner/outer loops) of these complex plane limaçon. The simulated points are plotted in red, and the best-fitted limaçon is represented by the blue curve. The illustration was performed for the following parameter values:  $N = 5, \gamma_x = 0.25, \gamma_y = 0.25, g_{xx} = 0.004/N, g_{yy} = 0.004/N, g_{xy} = 0.21875/N, g_{yx} = -0.08/N$ .

strengths  $g$  was necessary to obtain PSSI within this range. Moreover, as supported both numerically and analytically, the critical PSSI behavior scaled well with the network size—that is, as  $N$  increased, the connectivity parameters  $g$  needed to be maintained in an inverse proportion with  $N$  in order to preserve the linearity of the power spectrum.

In the original model, while the system's deterministic component is linear, other aspects of the process of obtaining the slopes  $\beta$  are highly nonlinear (e.g., the linear fit is performed under a log–log scale). So in the end, the linear dependence of the PSSI slopes on the two connectivity parameters (Fig. 5) is unexpected, and provides an additional direction for future investigation.

### Future directions

One general aim of this paper is to inform how fMRI can be used in conjunction with a theoretical model, in order to interpret the impact of connectivity on brain dynamics. Once established that a modeling approach can be useful in this context, one can explore selected biophysical aspects in greater detail.

For example, a widely accepted ratio of  $I:E = M_{yx}:M_{xy}$  in brain physiological networks is 15–20%. A particular  $M_{yx}:M_{xy}$  ratio can be, however, obtained in conjunction with various degrees of overall network connectivity (or total density  $M_{xy} + M_{yx}$ ). The network's coupling profile, and therefore its coupled dynamical behavior (in our model, as well as in real biophysical networks), depends not only on the ratio  $M_{yx}:M_{xy}$ , but also on the total connectivity, which may vary quite widely in real networks with their type, location and function. Our model's reference point of both  $E$  and  $I$  at 50% max (implying  $I:E = 1:1$ ), has a theoretical significance: that the excitation and inhibition are optimally balanced. This can be normalized (by retuning parameters) to the balance needed for the particular network at hand. This fine tuning will be incorporated in future iterations, with parameters estimated from data and used to reproduce a particular biophysical network.

With this in mind, we focused at this first stage on maintaining the model's generality, simplicity, and potential for extension. We analyzed a linear OU system, then a basic nonlinear extension of it; we considered input noise with very simple statistical features (Wiener process). Our framework can be used (by adjusting parameters and time scales) to describe dynamics at the spiking/synaptic level, at the firing rate/neural coupling level, or at the region of interest/hemodynamic connectivity level. For the empirical application in this paper, our model addresses the hemodynamic scale, so that nodes are to be viewed as the smaller functional partitions that form regions of interest, and their activation is consistent with voxel-wise time series from fMRI.

Some of our current work is focused on addressing in more analytical depth some of the mathematical aspects investigated numerically in this manuscript. Within the framework of our model of coupled nonlinear (Wilson–Cowan) oscillators, we are studying the changes in dynamics under perturbations of the coupling architecture. On one hand, we are investigating the spectral properties of the coupling (adjacency) graph, and the robustness of the eigenvalues to changes in edge density or configuration. We noticed that, within certain parameter ranges, the adjacency eigenvalues remain in general sufficiently robust to perturbations in edge geometry as long as the edge densities (as defined in this paper) do not change, suggesting that simple learning algorithms in such systems may also remain unaffected by constrained configuration changes. In parallel, we are also studying the phase-space dynamics of the system, and locating (using entropy, as well as Hopf and saddle-node bifurcation diagrams) its transitions between different dynamic regimes produced by perturbing the underlying graph. One of our main goals is to understand how changing the strengths, versus the density, versus the geometry of the connections can have completely different effects upon the coupled dynamics, although they seemingly accomplish the same task, of strengthening and/or weakening the coupling.

In developing future iterations of the model, it will also be important to use properties of random adjacency matrices and generalize to more than two inter-connected modules, in order to study classes of inhibitory vs. excitatory structures. The model also can relax the “fully-connectedness” condition currently assumed within each network module, to explore other geometric distributions of edges. We would expect that there might be two key conditions for optimal function in such networks: first, the requirement for a well-balanced adjacency matrix. The corresponding bidirectional graph should appropriately combine robust features (e.g., fully connected populations) and random edges (e.g., due to synaptic probing) so as to allow some flexibility, yet also render sufficient stability for convergence during a cognitive process such as learning. Second, there should be well-balanced connection strengths (i.e., the weights on each adjacency edge), hence an efficient connectivity matrix driving optimal dynamics in the system. We are currently studying spectra of more general adjacency matrices, and exploring different schemes of robust versus random components in the edge distribution, compatible with neural network properties observed in experimental recordings. Recent theories suggests that realistic complex behavior, comparable to neural behavior, cannot be obtained from either a too globally rigid structure, or from only locally-based connections (to a small number of neighboring nodes). A logical next step would be to use results from random matrix and graph theory, hybrid structures that can explore how scale-free and critical behavior might relate in the context of Erdős–Rényi modeling.

### Acknowledgments

This research was supported by the National Science Foundation (0954643 and 1141915; LRMP), the Office of Naval Research (N0014-04-1-005; LRMP) and the Burroughs Wellcome Fund (CRTG 1010138; AR). We would like to thank Aaron Clauset and Stephen Preston for our valuable discussions.

### Conflict of interest

The authors declare they have no conflict of interest.

### References

- Achard, S., Salvador, R., Whitcher, B., Suckling, J., Bullmore, E., 2006. A resilient, low-frequency, small-world human brain functional network with highly connected association cortical hubs. *J. Neurosci.* 26 (1), 63–72.
- Bär, K., Boettger, M., Koschke, M., Schulz, S., Chokka, P., Yeragani, V., Voss, A., 2007. Non-linear complexity measures of heart rate variability in acute schizophrenia. *Clin. Neurophysiol.* 118 (9), 2009–2015.
- Baxter, M., Parker, A., Lindner, C., Izquierdo, A., Murray, E., 2000. Control of response selection by reinforcer value requires interaction of amygdala and orbital prefrontal cortex. *J. Neurosci.* 20 (11), 4311–4319.
- Bhattacharya, J., et al., 2000. Complexity analysis of spontaneous EEG. *Acta Neurobiol. Exp.* 60 (4), 495–502.
- Bibbona, E., Panfilo, G., Tavella, P., 2008. The Ornstein–Uhlenbeck process as a model of a low pass filtered white noise. *Metrologia* 45, S117.
- Boccaletti, S., Latora, V., Moreno, Y., Chavez, M., Hwang, D.-U., 2006. Complex networks: structure and dynamics. *Phys. Rep.* 424 (4), 175–308.
- Borisjuk, G.N., Borisjuk, R.M., Khibnik, A.I., Roose, D., 1995. Dynamics and bifurcations of two coupled neural oscillators with different connection types. *Bull. Math. Biol.* 57 (6), 809–840.
- Brozović, M., Abbott, L., Andersen, R., 2008. Mechanism of gain modulation at single neuron and network levels. *J. Comput. Neurosci.* 25 (1), 158–168.
- Brunel, N., 2000. Dynamics of sparsely connected networks of excitatory and inhibitory spiking neurons. *J. Comput. Neurosci.* 8 (3), 183–208.
- Bruzzo, A., Gesierich, B., Santi, M., Tassinari, C., Birbaumer, N., Rubboli, G., 2008. Permutation entropy to detect vigilance changes and preictal states from scalp EEG in epileptic patients: a preliminary study. *Neurol. Sci.* 29 (1), 3–9.
- Bullmore, E., Sporns, O., 2009. Complex brain networks: graph theoretical analysis of structural and functional systems. *Nat. Rev. Neurosci.* 10 (3), 186–198.
- Buxton, R.B., Uludag, K., Dubowitz, D.J., Liu, T.T., 2004. Modeling the hemodynamic response to brain activation. *Neuroimage* 23 (Suppl. 1), S220–S233.
- Carlson, J., Greenberg, T., Rubin, D., Mujica-Parodi, L., 2011. Feeling anxious: anticipatory amygdalo-insular response predicts the feeling of anxious anticipation. *Soc. Cogn. Affect. Neurosci.* 6 (1), 74–81.

- Cerutti, S., Hoyer, D., Voss, A., 2009. Multiscale, multiorgan and multivariate complexity analyses of cardiovascular regulation. *Philos. Trans. R. Soc. A Math. Phys. Eng. Sci.* 367 (1892), 1337–1358.
- Ciucci, P., Varoquaux, G., Abry, P., Sadaghiani, S., Kleinschmidt, A., 2012. Scale-free and multifractal time dynamics of fMRI signals during rest and task. *Front. Physiol.* 3.
- Cordes, D., Haughton, V., Arfanakis, K., Carew, J., Turski, P., Moritz, C., Quigley, M., Meyerand, M., 2001. Frequencies contributing to functional connectivity in the cerebral cortex in resting-state data. *Am. J. Neuroradiol.* 22 (7), 1326–1333.
- Davis, M., Whalen, P., et al., 2001. The amygdala: vigilance and emotion. *Mol. Psychiatry* 6 (1), 13–34.
- Destexhe, A., Sejnowski, T.J., 2009. The Wilson–Cowan model, 36 years later. *Biol. Cybern.* 101 (1), 1–2.
- Faure, P., Korn, H., 2001. Is there chaos in the brain? I. concepts of nonlinear dynamics and methods of investigation. *C. R. Acad. Sci. III* 324 (9), 773–793.
- Freeman, B.N., Pasley, R.D., 2008. Neurovascular coupling. *Scholarpedia* 3 (3), 5340.
- Friston, K., Mechelli, A., Turner, R., Price, C., 2000. Nonlinear responses in fMRI: the balloon model, Volterra kernels, and other hemodynamics. *Neuroimage* 12 (4), 466–477.
- Friston, K., Harrison, L., Penny, W., 2003. Dynamic causal modelling. *Neuroimage* 19 (4), 1273–1302.
- Gisiger, T., 2001. Scale invariance in biology: coincidence or footprint of a universal mechanism? *Biol. Rev.* 76 (2), 161–209.
- Gray, R.T., Robinson, P.A., 2008. Stability and synchronization of random brain networks with a distribution of connection strengths. *Neurocomputing* 71 (7), 1373–1387.
- Gray, R.T., Robinson, P.A., 2009. Stability and structural constraints of random brain networks with excitatory and inhibitory neural populations. *J. Comput. Neurosci.* 27 (1), 81–101.
- He, B.J., 2011. Scale-free properties of the functional magnetic resonance imaging signal during rest and task. *J. Neurosci.* 31 (39), 13786–13795.
- He, Y., Evans, A., 2010. Graph theoretical modeling of brain connectivity. *Curr. Opin. Neurol.* 23 (4), 341.
- Ho, K., Moody, G., Peng, C., Mietus, J., Larson, M., Levy, D., Goldberger, A., 1997. Predicting survival in heart failure case and control subjects by use of fully automated methods for deriving nonlinear and conventional indices of heart rate dynamics. *Circulation* 96 (3), 842–848.
- Hodgkin, A., Huxley, A., 1952. Propagation of electrical signals along giant nerve fibres. *Proc. R. Soc. Lond. Ser. B Biol. Sci.* 140 (899), 177–183.
- Iturria-Medina, Y., Sotero, R., Canales-Rodríguez, E., Alemán-Gómez, Y., Melie-García, L., 2008. Studying the human brain anatomical network via diffusion-weighted MRI and graph theory. *Neuroimage* 40 (3), 1064–1076.
- Izquierdo, A., Murray, E., 2005. Opposing effects of amygdala and orbital prefrontal cortex lesions on the extinction of instrumental responding in macaque monkeys. *Eur. J. Neurosci.* 22 (9), 2341–2346.
- Juhász, F., 1990. On the characteristic values of non-symmetric block random matrices. *J. Theor. Probab.* 3 (2), 199–205.
- Kaplan, D., Furman, M., Pincus, S., Ryan, S., Lipsitz, L., Goldberger, A., 1991. Aging and the complexity of cardiovascular dynamics. *Biophys. J.* 59 (4), 945–949.
- Kellman, P., Gelderen, P., de Zwart, J., Duyn, J., 2003. Method for functional MRI mapping of nonlinear response. *Neuroimage* 19 (1), 190–199.
- Kloeden, P., Platen, E., Schurz, H., 1994. Stochastic differential equations. Numerical Solution of SDE Through Computer Experiments. 63–90.
- Korn, H., Faure, P., 2003. Is there chaos in the brain? II. Experimental evidence and related models. *C. R. Biol.* 326 (9), 787–840.
- Lai, M., Lombardo, M., Chakrabarti, B., Sadek, S., Pasco, G., Wheelwright, S., Bullmore, E., Baron-Cohen, S., Suckling, J., et al., 2010. A shift to randomness of brain oscillations in people with autism. *Biol. Psychiatry* 68 (12), 1092–1099.
- LeDoux, J., 2000. Emotion circuits in the brain. *Annu. Rev. Neurosci.* 23 (1), 155–184.
- Li, B., Freeman, R., 2007. High-resolution neurometabolic coupling in the lateral geniculate nucleus. *J. Neurosci.* 27 (38), 10223–10229.
- Li, J., Ning, X., Ma, O., 2007. Nonlinear dynamical complexity analysis of short-term heart-beat series using joint entropy. *J. Biomed. Eng.* 24 (2), 285.
- Logothetis, N., Pauls, J., Augath, M., Trinath, T., Oeltermann, A., et al., 2001. Neurophysiological investigation of the basis of the fMRI signal. *Nature* 412 (6843), 150–157.
- Mäkilä, T., Ristimäe, T., Airaksinen, K.E.J., Peng, C.K., Goldberger, A.L., Huikuri, H.V., et al., 1998. Heart rate dynamics in patients with stable angina pectoris and utility of fractal and complexity measures. *Am. J. Cardiol.* 81 (1), 27–31.
- Marreiros, A.C., Daunizeau, J., Kiebel, S.J., Friston, K.J., 2008. Population dynamics: variance and the sigmoid activation function. *Neuroimage* 42 (1), 147–157.
- Mitra, P., Bokil, H., 2007. Observed Brain Dynamics. Oxford University Press, USA.
- Molteni, E., Perego, P., Zanotta, N., Reni, G., 2008. Entropy analysis on EEG signal in a case study of focal myoclonus. *Engineering in Medicine and Biology Society*, 2008. EMBS 2008. 30th Annual International Conference of the IEEE. IEEE, pp. 4724–4727.
- Monahan, A., 1998. Stochastic Differential Equations: A Sad Primer. Lecture Notes. University of British Columbia, Vancouver, Canada.
- Mujica-Parodi, L., Yeragani, V., Malaspina, D., 2005. Nonlinear complexity and spectral analyses of heart rate variability in medicated and unmedicated patients with schizophrenia. *Neuropsychobiology* 51 (1), 10–15.
- Mujica-Parodi, L., Korgaonkar, M., Ravindranath, B., Greenberg, T., Tomasi, D., Wagshul, M., Ardekani, B., Guilfoyle, D., Khan, S., Zhong, Y., et al., 2009. Limbic dysregulation is associated with lowered heart rate variability and increased trait anxiety in healthy adults. *Hum. Brain Mapp.* 30 (1), 47–58.
- O'Reilly, R., Frank, M., 2006. Making working memory work: a computational model of learning in the prefrontal cortex and basal ganglia. *Neural Comput.* 18 (2), 283–328.
- Ogawa, S., Lee, T., Stepanoski, R., Chen, W., Zhu, X., Ugurbil, K., 2000. An approach to probe some neural systems interaction by functional MRI at neural time scale down to milliseconds. *Proc. Natl. Acad. Sci.* 97 (20), 11026.
- Pasemann, F., 1993. Dynamics of a single model neuron. *Int. J. Bifurcation Chaos* 3, 271–278.
- Peng, C., Mietus, J., Hausdorff, J., Havlin, S., Stanley, H., Goldberger, A., 1993. Long-range anticorrelations and non-Gaussian behavior of the heartbeat. *Phys. Rev. Lett.* 70 (9), 1343.
- Peng, C., Buldyrev, S., Hausdorff, J., Havlin, S., Mietus, J., Simons, M., Stanley, H., Goldberger, A., 1994. Non-equilibrium dynamics as an indispensable characteristic of a healthy biological system. *Integr. Psychol. Behav. Sci.* 29 (3), 283–293.
- Peng, C., Havlin, S., Stanley, H., Goldberger, A., 1995. Quantification of scaling exponents and crossover phenomena in nonstationary heartbeat time series. *Chaos* 5 (1), 82–87.
- Phelps, E., Delgado, M., Nearing, K., LeDoux, J., 2004. Extinction learning in humans: role of the amygdala and vmPFC. *Neuron* 43 (6), 897–905.
- Pincus, S., Goldberger, A., 1994. Physiological time-series analysis: what does regularity quantify? *Am. J. Physiol. Heart Circ. Physiol.* 266 (4), H1643–H1656.
- Protzner, A., Valliant, T., Kovacevic, N., McCormick, C., McAndrews, M., 2010. Hippocampal signal complexity in mesial temporal lobe epilepsy: a noisy brain is a healthy brain. *Arch. Ital. Biol.* 148 (3), 289.
- Rădulescu, A., 2008. Schizophrenia—a parameters game? *J. Theor. Biol.* 254 (1), 89–98.
- Rădulescu, A., 2009. A multi-etiology model of systemic degeneration in schizophrenia. *J. Theor. Biol.* 259 (2), 269–279.
- Rădulescu, A., Rubin, D., Strey, H., Mujica-Parodi, L., 2012. Power spectrum scale invariance identifies prefrontal dysregulation in paranoid schizophrenia. *Hum. Brain Mapp.* 33 (7), 1582–1593.
- Ricciardi, L., Sacerdote, L., 1979. The Ornstein–Uhlenbeck process as a model for neuronal activity. *Biol. Cybern.* 35 (1), 1–9.
- Rosa, M.J., Kilner, J.M., Penny, W.D., 2011. Bayesian comparison of neurovascular coupling models using EEG–fMRI. *PLoS Comput. Biol.* 7 (6), e1002070.
- Rosenkranz, J., Moore, H., Grace, A., 2003. The prefrontal cortex regulates lateral amygdala neuronal plasticity and responses to previously conditioned stimuli. *J. Neurosci.* 23 (35), 11054–11064.
- Rubin, D., Fekete, T., Mujica-Parodi, L.R., 2013. Optimizing complexity measures for fMRI data: algorithm, artifact, and sensitivity. *PLoS One* 8 (5), e63448.
- Sheth, S., Nemoto, M., Guiou, M., Walker, M., Pouratian, N., Toga, A., 2004. Linear and nonlinear relationships between neuronal activity, oxygen metabolism, and hemodynamic responses. *Neuron* 42 (2), 347–355.
- Siri, B., Quoy, M., Delord, B., Cessac, B., Berry, H., 2007. Effects of Hebbian learning on the dynamics and structure of random networks with inhibitory and excitatory neurons. *J. Physiol. Paris* 101 (1), 136–148.
- Sotres-Bayon, F., Cain, C., LeDoux, J., 2006. Brain mechanisms of fear extinction: historical perspectives on the contribution of prefrontal cortex. *Biol. Psychiatry* 60 (4), 329–336.
- Sporns, O., 2010. Networks of the Brain. The MIT Press.
- Stanley, H., Buldyrev, S., Goldberger, A., Hausdorff, J., Havlin, S., Mietus, J., Peng, C., Sciortino, F., Simons, M., 1992. Fractal landscapes in biological systems: long-range correlations in DNA and interbeat heart intervals. *Physica A* 191 (1), 1–12.
- Stephan, K., Weiskopf, N., Drysdale, P., Robinson, P., Friston, K., 2007. Comparing hemodynamic models with DCM. *Neuroimage* 38 (3), 387–401.
- Tolkunov, D., Rubin, D., Mujica-Parodi, L., 2010. Power spectrum scale invariance quantifies limbic dysregulation in trait anxious adults using fMRI: adapting methods optimized for characterizing autonomic dysregulation to neural dynamic time series. *Neuroimage* 50 (1), 72–80.
- Valencia, J., Vallverdú, M., Schroeder, R., Voss, A., Vázquez, R., Bayes de Luna, A., Caminal, P., 2009. Complexity of the short-term heart-rate variability. *Eng. Med. Biol. Mag. IEEE* 28 (6), 72–78.
- Vazquez, A.L., Noll, D.C., 1998. Nonlinear aspects of the bold response in functional MRI. *Neuroimage* 7 (2), 108–118.
- Ventura, J., Liberman, R., Green, M., Shaner, A., Mintz, J., 1998. Training and quality assurance with the structured clinical interview for DSM-IV (SCID-I/P). *Psychiatry Res.* 79 (2), 163–173.
- Voss, A., Kurths, J., Kleiner, H., Witt, A., Wessel, N., 1995. Improved analysis of heart rate variability by methods of nonlinear dynamics. *J. Electrocardiol.* 28, 81–88.
- Wilson, H.R., Cowan, J.D., 1972. Excitatory and inhibitory interactions in localized populations of model neurons. *Biophys. J.* 12 (1), 1–24.
- Xu, N.-I., Harnett, M.T., Williams, S.R., Huber, D., O'Connor, D.H., Svoboda, K., Magee, J.C., 2012. Nonlinear dendritic integration of sensory and motor input during an active sensing task. *Nature* 492, 247–251.
- Zarahn, E., Aguirre, G., d'Esposito, M., 1997. Empirical analyses of bold fMRI statistics. *Neuroimage* 5 (3), 179–197.